



# CHORUS

This is the accepted manuscript made available via CHORUS. The article has been published as:

## Large-eddy simulation of turbulent flow over spanwise-offset barchan dunes: Interdune vortex stretching drives asymmetric erosion

Chao Wang and William Anderson

Phys. Rev. E **98**, 033112 — Published 18 September 2018

DOI: [10.1103/PhysRevE.98.033112](https://doi.org/10.1103/PhysRevE.98.033112)

1 **Large-eddy simulation of turbulent flow over spanwise-offset barchan dunes: interdune**  
2 **vortex stretching drives asymmetric erosion**

3 Chao Wang

4 *Mechanical Engineering Department,*  
5 *The University of Texas at Dallas*  
6

7 William Anderson\*

8 *Mechanical Engineering Department, The University of Texas at Dallas*

9 (Dated: August 24, 2018)

10 The coupling between turbulent flow physics and barchan dune geometry is important to dune  
11 migration, morphology of individual dunes, and the morphodynamics of merging and separating  
12 proximal dunes. Large-eddy simulation was used to model turbulent, inertial-dominated flow over  
13 a series of static barchan dune configurations. The dune configurations were carefully designed to  
14 capture realistic stages of a so-called “offset interaction”, wherein a small dune is placed upflow  
15 of a relatively larger dune, thereby guaranteeing interaction since the former migrates faster than  
16 the latter. Moreover, as interaction proceeds, the morphology of the small dune is mostly pre-  
17 served, while the large dune undergoes dramatic transformation with greater erosion downflow of  
18 the interdune space. Simulations reveal that the wake centerline – determined here as the spanwise  
19 location at which the momentum deficit associated with each dune exhibits a minimum – veers due  
20 to dune geometry. Visualization of vortex identifiers reveals that hairpin vortices are produced via  
21 separation across the crestline of dunes, and these hairpins are advected downflow by the prevailing,  
22 background flow. The legs of hairpins emanating from the upflow dune contain streamwise vorticity  
23 of opposite sign, wherein the hairpin leg within the interdune space exhibits positive streamwise  
24 vorticity. This positive streamwise vorticity is supplied to the interdune space, where flow chan-  
25 neling induces acceleration of streamwise velocity. An assessment of right-hand side terms of the  
26 Reynolds-averaged streamwise vorticity transport equation confirm, indeed, that vortex stretching  
27 is the dominant contributor to sustenance of streamwise vorticity. With this, we can conclude  
28 that asymmetry of the large, downflow dune is a consequence of scour due to the interdune roller,  
29 and scouring intensifies as the spacing between dunes decreases. A structural model outlining this  
30 process is presented.

31 **Usage:** Turbulence, barchan dune, interaction, aeolian

32 **PACS numbers:** May be entered using the `\pacs{#1}` command.

33 **Structure:** You may use the `description` environment to structure your abstract; use the optional argument of  
34 the `\item` command to give the category of each item.

---

\* Corresponding author email: wca140030@utdallas.edu

## I. INTRODUCTION

The feedback between imposed aero-/hydro-dynamic loading and sand dune geometry is a control on sand dune morphology and the spatial migration rate of dunes [1–14], since sediment transport is the product of surface stress imposed by the above fluid. Under the inertial-dominated conditions typical of the atmospheric surface layer (ASL) [2, 12, 15, 16] or the roughness sublayer of aquatic flows over river dunes [4], surface stress is dominated by turbulence [17] and, therefore,  $\tau^w \sim u^2$ , where  $\tau^w$  is surface stress and  $u$  is the dominant component of the velocity vector,  $\mathbf{u}$  [18]. Since sediment (saltation) mass flux,  $q$ , scales non-linearly with shear velocity,  $q \sim u_*^n$ , and because  $\tau^w \sim u_*^2 \sim u^2$ , it follows that  $q \sim u^n$  [1, 19–21]. Although specific values for scaling exponent,  $n$ , vary,  $n = 3$  is commonly cited [20, 21], which demonstrates the extent to which dune morphodynamics are influenced by turbulent fluctuations. Some very recent studies have reported stronger support for  $n = 2$ , but this still demonstrates the importance of turbulent fluctuations [22, 23]. In this work, large-eddy simulation (LES) has been used to model flow over a stages of a dune interaction; rigorous assessment of turbulent processes responsible for sustenance of vortical flow structures – and their role in advancing the interaction – have been performed. Note that in this work, the flow is assumed to be incompressible, and thus flow quantities are considered on a density-normalized basis. In the interest of generality, therefore, we will refer to the “upflow” and “downflow” direction throughout [12, 24].

### A. Background

Dune morphology is controlled by a range of parameters [25], or boundary conditions, although for the present article we focus on prevailing flow direction (other factors, including soil moisture and vegetation, can stabilize dunes and alter their geometry, but such influences are not considered for this study). Variability in wind direction – whether associated with local processes, or with processes occurring over diurnal, seasonal, or larger-scale climatic oscillations – alters barchan dune morphology and can result in crescentic, linear, or star dunes [1, 2, 26–29]. Under the action of a unidirectional flow, canonical barchan dunes in isolation form and migrate in the downflow direction [30, 31]. The prevailing flow direction is coaligned with the  $x$ -axis (in this article, the first, second, and third component of any vector corresponds with its value in the streamwise, spanwise, and vertical direction, respectively, including the Euclidian vector,  $\mathbf{x} = \{x, y, z\}$ ). Isolated barchans are defined by centerline symmetry about the streamwise-vertical plane, with limbs of sediment extending in the downflow direction, but symmetry rapidly breaks down with even modest flow variability [32]. Herein, we focus on morphodynamic changes associated with local flow variability due to the presence of proximal dunes.

Dune migration is the product of cumulative grain transport, with individual grains saltating over the windward (stoss) side before careering down the lee side via avalanche. It follows, then, that the migration rate is inversely proportional to dune volume,  $\mathcal{V} = \int_{\mathcal{A}} h(\mathbf{x}) d^2 \mathbf{x}$ , where  $\mathcal{A}$  and  $h(\mathbf{x})$  is the  $x - y$  plane and digital elevation model of an individual dune, respectively. Thus, for a field composed of a spectrum of dune sizes, the preceding volume-migration proportionality argument demonstrates that dunes are likely to collide, or interact, as the trajectory of smaller and larger dunes overlap [26, 27, 33]. Aloft and downflow of individual dunes, the flow is greatly perturbed by individual dunes (this is true of the mean, or Reynolds-averaged flow, and fluctuations superimposed upon the Reynolds average). Thus, in the context of the driving flow, dune interactions are likely to begin long before dune junctions occur.

Owing to the number of parameters affecting dune morphodynamics, and the capacity for parameters to vary in space and time, natural dune fields exhibit geometric complexity over a range of scales [25]. Large-scale computer simulation of flow over a dune field – i.e., one with spatial extent in the horizontal direction many times larger than the depth of the aloft flow – would present a substantial computational challenge. Indeed, Khosronejad and Sotiropoulos (2014) [13] recently used a coupled morphodynamic solver to dynamically capture key aspects of dune genesis, evolution, and dune field self organization [34–39]; their results agreed favorably with flume results from Venditti et al. [40–43]. For the present work, however, we focused on a building-block interaction, which exists as part of a larger set of canonical interactions [26]: the offset merger interaction. We have used a series of high-fidelity diagnostic techniques to explain how, and why, this interaction advances.

Figure 1 shows instantaneous photographs of an offset merger interaction, recorded during flume experiments by Hersen and Douady (2005) [31]. For these images, a unidirectional flow induces migration of a relatively small and large barchan, where the former is placed upflow of the latter, thereby guaranteeing interaction. As time advances, the small dune approaches the large dune, while morphology of the former exhibits no discernible time dependence. The larger downflow dune, on the other hand, undergoes a major transformation as time advances. The horn of the downflow dune coaligned with the trajectory of the upflow dune is elongated, with the dune becoming more asymmetric as the upflow spacing diminishes (the term “horn” is used to denote the lateral extremities of barchan dunes).

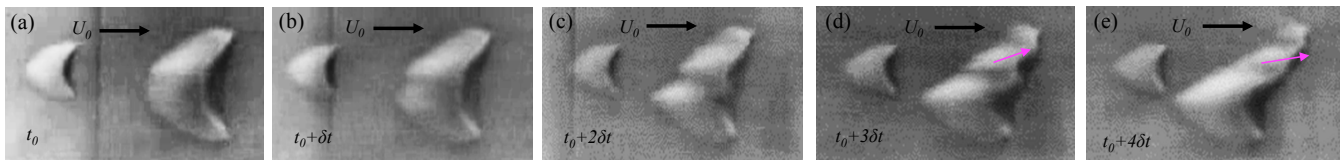


FIG. 1. Photographs of offset merger interaction stages [26], observed in mobile-bed flume experiments (images retrieved from Hersen and Douady, 2005 [31]). Annotations of prevailing mean flow direction and representative times added for illustration; red arrows illustrate downflow trajectory of ejected dune, or the “ejecta” [25].

88

## B. Prior work

89 In a preceding article [24], we considered four static dune topographies inspired by the Figure 1 series. In that study,  
 90 experimental measurements and LES runs were used to highlight the presence of a channeling flow in the interdune  
 91 space between the upflow and downflow dune. Analysis of the mean flow resulted in illustration that the wake of the  
 92 upflow and downflow dunes is not coaligned with the streamwise direction, but instead veers. This was referred to  
 93 as “wake veering”: the wake veering profiles between experiments and simulations agreed closely, and we reported a  
 94 trend of monotonically increasing spanwise veering of wakes as dune spacing decreases (discussion to follow in text  
 95 accompanying Figures 4g and h).

96 In our previous study [24], the large downflow dune was symmetric about the centerline for all four cases, though  
 97 Figure 1 shows that this is an incorrect depiction of the morphological realizations exhibited as an actual offset-merger  
 98 interaction advances [14]. Moreover, we did not determine the *driving mechanism* responsible for the flow channeling.  
 99 That is: what processes in the interdune space are responsible for sustenance of the channeling, and why do these  
 100 processes intensify as proximal dune spacing declines?

101 With these questions, six static dune configurations have been considered for the present article. The configurations  
 102 were carefully selected to mimic stages from the series of photographs in Figure 1, and are illustrated in Figure 2.  
 103 Comprehensive discussion of the cases is provided below, but here we mention a few key attributes. First, Case S1  
 104 features an isolated barchan, which serves as a basis for comparison against Cases S2 to S4 (Figure 2a). Cases S3’  
 105 and S4’, shown in Figures 2(b) and 2(c), respectively, feature an asymmetric large downflow dune with small upflow  
 106 dune at declining streamwise spacing. On Figure 2(a), annotations of the spanwise offset,  $s_y/h$ , and streamwise offset,  
 107  $s_x/h$ , are shown, while the level of asymmetry,  $\Delta x/h$ , is sketched on Figure 2(b,c). The inclusion of Cases S3’ and S4’  
 108 provides far greater generality by virtue of the asymmetry,  $\Delta x/h$ , that is a clear manifestation of the offset merger  
 109 interaction (Figure 1). Cases S5 and S6 are high-resolution versions of S2 and S4, respectively, and are included to  
 110 demonstrate that the simulations are not affected by resolution. Since no resolution sensitivity is reported for these  
 111 cases, we declined to assess resolution sensitivity for other cases.

112

## C. This study

113 LES has been used to model inertial-dominated flow over the cases depicted in Figure 2. This work is an extension  
 114 of the findings from our previous article [24], but herein we have used post-processing tools to fully elucidate the  
 115 driving mechanisms responsible for the morphodynamics observed in Figure 1; moreover, we consider additional cases  
 116 that capture the actual spatial asymmetry exhibited by the large downflow dune.

117 In Section II, we present the LES code, while in Section III we provide comprehensive description of the dune cases.  
 118 In Section IV, results directly retrieved from the simulations (and derived from rigorous post processing) are presented.  
 119 The results culminate in presentation of a model for flow structures within the interdune space and explanation of their  
 120 role in driving the asymmetric morphology of the large, downflow dune. Specifically, we demonstrate that streamwise  
 121 vorticity embodied within the legs of hairpins shed from the small dune are supplied to the interdune space – where  
 122 flow channeling forces a streamwise gradient in streamwise velocity – which yields vortex stretching and sustains the  
 123 interdune roller. Concluding remarks are provided in Section V.

124 We must emphasize that the present study considers static dunes, and the simulations include no sediment-fluid  
 125 morphodynamic coupling. In recent times, others have made major contributions in this area: for example, consider  
 126 the work of Ortiz and Smolarkiewicz [44] or, more recently, Khosronejad and Sotiropoulos [13], where the former  
 127 group modeled morphodynamic evolution of a barchan under unidirectional flow while the latter group predicted  
 128 evolution of an actual dune field. As opposed to Khosronejad and Sotiropoulos [13], who considered evolution of a  
 129 field of dunes, in this article we adopted a “building block” approach, choosing instead to discern driving mechanisms

TABLE I. Summary of simulation attributes ( $H = 100$  m,  $u_{*,d} = 0.45$  m.s $^{-1}$ ) and dune field configurations considered for present article.

Case	$N_x$	$N_y$	$N_z$	$L_x/H$	$L_y/H$	$L_z/H$	$\hat{z}_0/H$	$\delta_t u_{*,d} H^{-1}$	$TU_0/H$	$h/H$	$s_x/h$	$s_y/h$	$\chi^a$	$\Delta x/h$
S1	128	128	128	4	4	1	$1 \times 10^{-5}$	$4.5 \times 10^{-5}$	1820.7	0.25	0.0	0.0	0.125	0.0
S2	128	128	128	4	4	1	$1 \times 10^{-5}$	$4.5 \times 10^{-5}$	1765.4	0.25	5.0	1.3	0.125	0.0
S3	128	128	128	4	4	1	$1 \times 10^{-5}$	$4.5 \times 10^{-5}$	1767.4	0.25	4.0	1.3	0.125	0.0
S4	128	128	128	4	4	1	$1 \times 10^{-5}$	$4.5 \times 10^{-5}$	1770.0	0.25	3.0	1.3	0.125	0.0
S3'	128	128	128	4	4	1	$1 \times 10^{-5}$	$4.5 \times 10^{-5}$	1769.9	0.25	4.0	1.3	0.125	1.0
S4'	128	128	128	4	4	1	$1 \times 10^{-5}$	$4.5 \times 10^{-5}$	1764.5	0.25	3.0	1.3	0.125	2.0
S5	256	256	256	4	4	1	$1 \times 10^{-5}$	$2.25 \times 10^{-5}$	1532.2	0.25	5.0	1.3	0.125	0.0
S6	256	256	256	4	4	1	$1 \times 10^{-5}$	$2.25 \times 10^{-5}$	1541.0	0.25	3.0	1.3	0.125	0.0

<sup>a</sup> Volume ratio,  $\chi = \mathcal{V}_s/\mathcal{V}_L$ , where  $\mathcal{V}_s$  and  $\mathcal{V}_L$  is volume of small and large dune, respectively.

responsible for one interaction. This approach is nonetheless relevant since, to our knowledge, detailed assessment of mechanisms driving the interdune rollers – which, as will be shown, are paramount during the interaction – has not been performed.

## II. LARGE-EDDY SIMULATION

During LES, the three-dimensional transport equation for grid-filtered, incompressible momentum is solved:  $D_t \tilde{\mathbf{u}}(\mathbf{x}, t) = \mathbf{f}(\mathbf{x}, t)$ , where  $\mathbf{f}(\mathbf{x}, t)$  is a collection of forces (pressure correction, pressure gradient, stress heterogeneity, and obstacle forces), and  $\tilde{\cdot}$  denotes a grid-filtered quantity. The grid-filtering operation is attained here via convolution with the spatial filtering kernel,  $\tilde{\mathbf{u}}(\mathbf{x}, t) = G_\Delta \star \mathbf{u}(\mathbf{x}, t)$ , where  $\Delta$  is the filter scale [45]. The grid-filtering operation yields a right-hand side forcing term,  $-\nabla \cdot \mathbf{T}$ , where  $\mathbf{T} = \langle \mathbf{u}' \otimes \mathbf{u}' \rangle_t$  is the subgrid-scale stress tensor and  $\langle \cdot \rangle_a$  denotes averaging over dimension,  $a$  (in this article, rank-1 and -2 tensors are denoted with bold-italic and bold-sans relief, respectively).

For the present study,  $D_t \tilde{\mathbf{u}}(\mathbf{x}, t) = \mathbf{f}(\mathbf{x}, t)$  is solved for a channel-flow arrangement [12, 46], with the flow forced by a pressure gradient,  $\mathbf{\Pi} = \{\Pi, 0, 0\}$ , where  $\Pi = [dP_0/dx] \frac{H}{\rho} = \tau^w/\rho = u_*^2 = 1$ , which sets the shear velocity,  $u_*$ , upon which all velocities are scaled ( $H$  is the surface layer depth and  $\tau^w$  is surface stress).  $D_t \tilde{\mathbf{u}}(\mathbf{x}, t) = \mathbf{f}(\mathbf{x}, t)$  is solved for high-Reynolds number, fully-rough conditions [18], and thus,  $\nu \nabla^2 \tilde{\mathbf{u}}(\mathbf{x}, t) = 0$ . Under the presumption of  $\rho(\mathbf{x}, t) \rightarrow \rho$ , the velocity vector is solenoidal,  $\nabla \cdot \tilde{\mathbf{u}}(\mathbf{x}, t) = 0$ . During LES, the (dynamic) pressure needed to preserve  $\nabla \cdot \tilde{\mathbf{u}}(\mathbf{x}, t) = 0$  is computed by computation of  $\nabla \cdot [D_t \tilde{\mathbf{u}}(\mathbf{x}, t) = \mathbf{f}(\mathbf{x}, t)]$  and imposing  $\nabla \cdot \tilde{\mathbf{u}}(\mathbf{x}, t) = 0$ , which yields a resultant pressure Poisson equation.

The channel-flow configuration is created by the aforementioned pressure-gradient forcing, and the following boundary condition prescription: at the domain top, the zero-stress Neumann boundary condition is imposed on streamwise and spanwise velocity,  $\partial \tilde{u}/\partial z|_{z/H=1} = \partial \tilde{v}/\partial z|_{z/H=1} = 0$ . The zero vertical velocity condition is imposed at the domain top and bottom,  $\tilde{w}(x, y, z/H = 0) = \tilde{w}(x, y, z/H = 1) = 0$ . Spectral discretization is used in the horizontal directions, thus imposing periodic boundary conditions on the vertical “faces” of the domain. The code uses a staggered-grid formulation [46], where the first grid points for  $\tilde{u}(\mathbf{x}, t)$  and  $\tilde{v}(\mathbf{x}, t)$  are located at  $\delta z/2$ , where  $\delta z = H/N_z$  is the resolution of the computational mesh in the vertical ( $N_z$  is the number of vertical grid points). Grid resolution in the streamwise and spanwise direction is  $\delta x = L_x/N_x$  and  $\delta y = L_y/N_y$ , respectively, where  $L$  and  $N$  denote horizontal domain extent and corresponding number of grid points, respectively (subscript  $x$  or  $y$  denotes streamwise or spanwise direction, respectively). Table I provides a summary of the domain attributes for the different cases, where the domain height has been set to the depth of the surface layer,  $L_z/H = 1$ .

At the lower boundary, surface momentum fluxes are prescribed with a hybrid scheme leveraging an immersed-boundary method (IBM) [47, 48] and the equilibrium logarithmic model [49], depending on the digital elevation model,  $h(x, y)$ . When  $h(x, y) < \delta z/2$ , the topography is vertically unresolved, and the logarithmic law is used:

$$\tau_{xz}^w(x, y, t) = - \left[ \frac{\kappa U(x, y, t)}{\log(\frac{1}{2}\delta z/\hat{z}_0)} \right]^2 \frac{\tilde{u}(x, y, \frac{1}{2}\delta z, t)}{U(x, y, t)} \quad (1)$$

and

$$\tau_{yz}^w(x, y, t) = - \left[ \frac{\kappa U(x, y, t)}{\log(\frac{1}{2}\delta z/\hat{z}_0)} \right]^2 \frac{\tilde{v}(x, y, \frac{1}{2}\delta z, t)}{U(x, y, t)} \quad (2)$$

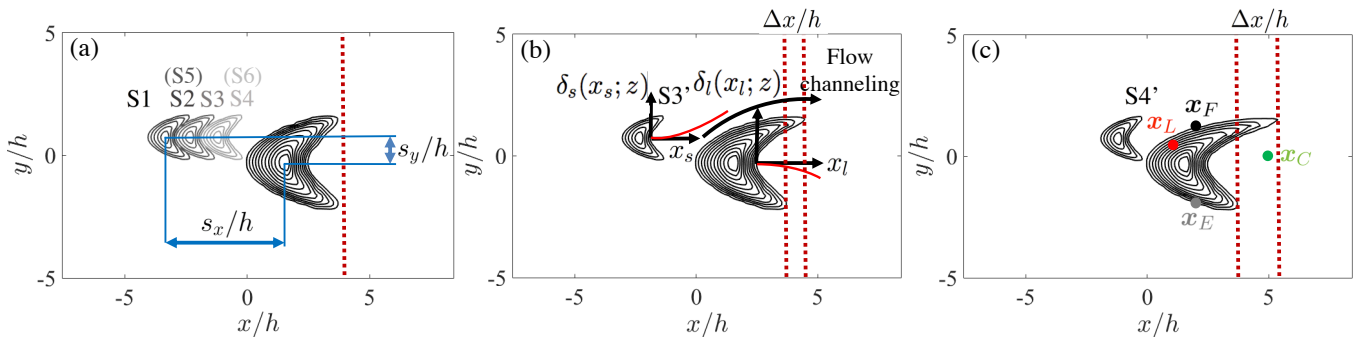


FIG. 2. Visualization of dune configurations considered for this study. Panel (a) shows Cases S1 to S4, Panel (b) shows Case S3', and Panel (c) shows Case S4' (see Table I for summary of simulation and geometric attributes). For visualization purposes, streamwise and spanwise position have been normalized by large dune crest height,  $h$ . Panel (a) includes annotation of streamwise offset,  $s_x/h$ , spanwise offset,  $s_y/h$ , and streamwise asymmetry,  $\Delta x/h$ . Cases S3' and S4' are equivalent to S3 and S4, respectively, with the exception of  $\Delta x/h$  streamwise asymmetry. Recall Figure 1, which shows how the large downflow dune horn exhibits asymmetric elongation as the upflow dune approaches [38], which is why we have considered S3' and S4'. In all cases (except S1), the upflow dune is equivalent, and a ratio of the small dune volume is computed and provided in Table I, where  $\chi = \mathcal{V}_s/\mathcal{V}_L$ , and where  $\mathcal{V}_s$  and  $\mathcal{V}_L$  is the volume associated with the small and large dune, respectively. Panel (b) annotations show local coordinates,  $x_s$  and  $x_l$ , used to quantify dune wakes,  $\delta_s(x_s; z)$  and  $\delta_l(x_l; z)$  (red lines). Solid black arrow denotes flow channeling. Panel (c) shows discrete locations (solid circles) used for time-series sampling of flow quantities, where  $\mathbf{x}_L/h = \{1, 0.5, 0.5\}$ ,  $\mathbf{x}_C/h = \{5, 0, 0.5\}$ ,  $\mathbf{x}_E/h = \{2, -2, z/h\}$ , and  $\mathbf{x}_F/h = \{2, 1.3, z/h\}$ . Table I gives detailed attributes of each case. Note, finally, that the small dune crest height is denoted by  $h_s$ . Individual dune digital elevation models provided by K. Christensen, Notre Dame, and used in recent articles [11, 14, 24].

165 where  $\hat{z}_0/H = 1 \times 10^{-5}$  is a prescribed roughness length (summarized in Table I),  $\bar{\cdot}$  denotes test-filtering [50, 51] (used  
 166 here to attenuate unphysical local surface stress fluctuations associated with localized application of Equation 1 and 2  
 167 [52]), and  $U(x, y, \frac{1}{2}\delta z, t) = (\bar{u}(x, y, \frac{1}{2}\delta z, t)^2 + \bar{v}(x, y, \frac{1}{2}\delta z, t)^2)^{1/2}$  is magnitude of the horizontal components of the test-  
 168 filtered velocity vector. Wherever  $h(x, y) > \frac{1}{2}\delta z$ , a continuous forcing IBM is used [48, 53], which has been successfully  
 169 used in similar studies of turbulent obstructed shear flows [12, 54, 55]. The IBM computes a body force,  $\mathbf{f}(x, t)$ , which  
 170 imposes circumferential momentum fluxes at computational “cut” cells based on spatial gradients of  $h(x, y)$ . Equations  
 171 1 and 2 are needed to ensure surface stress is imposed when  $h(x, y) < \frac{1}{2}\delta z$ . Subgrid-scale stresses are modeled with  
 172 an eddy-viscosity model,  $\boldsymbol{\tau}^d = -2\nu_t \mathbf{S}$ , where  $\mathbf{S} = \frac{1}{2}(\nabla \tilde{\mathbf{u}} + \nabla \tilde{\mathbf{u}}^T)$  is the resolved strain-rate tensor. The eddy viscosity  
 173 is  $\nu_t = (C_s \Delta)^2 |\mathbf{S}|$ , where  $|\mathbf{S}| = (2\mathbf{S} : \mathbf{S})^{1/2}$ ,  $C_s$  is the Smagorinsky coefficient, and  $\Delta$  is the grid resolution. For  
 174 the present simulations, the Lagrangian scale-dependent dynamic model is used [52] to assess  $C_s$  during LES. The  
 175 simulations have been run for  $N_t \delta_t U_0 u_{*,d} H^{-1} \approx 10^3$  large-eddy turnovers, where  $U_0 = \langle \tilde{u}(x, y, (L_z - \delta z/2)/H = 1, t) \rangle_t$   
 176 is a “freestream” or centerline velocity. This duration is sufficient for computation of Reynolds-averaged quantities  
 177 (specific values are reported in Table I).

178 Note that the  $u_{*,d}$  and  $H$  cited in Table I are used only to normalize the dimensional time,  $\delta t^* = \delta t u_* H^{-1}$ . For  
 179 all other purposes, flow quantities are normalized by the LES friction velocity,  $u_*$ , which is derived by the imposed  
 180 (and non dimensional) pressure gradient, as per the text at the opening of this section. Owing to this approach, and  
 181 due to the inertial-dominated state attained under fully-rough flow conditions, the LES-derived flow statistics will  
 182 exhibit dynamic similarity with flows in the atmospheric surface layer, the roughness sublayer of hydraulic flows, or  
 183 laboratory flows in flumes or wind tunnels.

### 184 III. CASES

185 Cases S1 to S4 are shown in Figure 2(a), Case S3' is shown in Figure 2(b), and Case S4' is shown in Figure 2(c).  
 186 Cases S5 and S6 have identical topographic attributes to Cases S2 and S4, respectively, but are projected upon a  
 187 relatively higher-resolution computational mesh (see Table I for simulation details). Cases S5 and S6 are included  
 188 for the purpose of resolution sensitivity assessment; results confirm that computational resolution has no discernible  
 189 effect on the results. For Cases S1 to S4, S5, and S6, the topographies are composed of streamwise-symmetric dunes,  
 190 where Case S1 is a single isolated dune. For Cases S2 to S4, S5, and S6, the large central dune from Case S1 is  
 191 retained, and an additional small dune is placed at a series of upflow locations,  $s_x/h$ , from a spanwise-offset position,  
 192  $s_y/h$ , where  $h$  is the crest height of the large dune (for perspective, horizontal position is normalized by  $h$  for Figure

193 2 and subsequent figures). Note that the streamwise and spanwise offsets are recorded in Table I. Note also that for  
 194 Figure 2 and subsequent figures, we have shifted the coordinate origin to the farthest upflow point of the large dune  
 195 (colloquially referred to as the “toe”), which helps to visualize the digital elevation models and flow fields.

196 The topographic configurations are intended to capture instantaneous morphodynamic realizations of an actual  
 197 offset-merger interaction, though Figure 1 shows that the large dune changes profoundly as the smaller upflow dune  
 198 approaches. For this reason, two additional cases – S3’ (Figure 2b) and S4’ (Figure 2c) – are considered, wherein the  
 199 large downflow dune exhibits the spanwise asymmetry that is characteristic of this particular interaction. The level  
 200 of asymmetry is quantified by parameter,  $\Delta x$ , and is annotated on Figure 2(b,c) (since Cases S1 - S4 correspond with  
 201 a symmetric dune,  $\Delta x = 0$  for these cases). By using high-fidelity LES to model turbulent flow over these cases, we  
 202 can study flow physics aloft the dunes and explain why the dune interaction advances as observed in Figure 1.

203 For Cases S2 - S4, S3’, and S4’, the height of the small dune is precisely half the height of the larger downflow dune.  
 204 For perspective, we construct the volumetric ratio,  $\chi = \mathcal{V}_s/\mathcal{V}_L = \int_{\mathcal{A}_s} h(\mathbf{x})d^2\mathbf{x}/\int_{\mathcal{A}_L} h(\mathbf{x})d^2\mathbf{x}$ , where subscripts “s”  
 205 and “L” denote small and large dune, respectively. For all the cases considered in this article,  $\chi = 1/8$ . Note that,  
 206 to an extent not considered here, Cases S1 - S4 were considered in our recent article [24]. But, in the present work,  
 207 we have considered additional cases that match actual morphodynamic realizations – S3’ and S4’ – and we perform  
 208 in-depth post-processing analyses that provide deeper insights into the aero-/hydro-dynamic processes sustaining this  
 209 interaction.

210 Note that the annotations on Figure 2(b) –  $x_s$ ,  $\delta_s(x_s; z)$ ,  $x_l$ , and  $\delta_l(x_l; z)$  – relate to the so-called wake-veering  
 211 phenomenon, which was presented in our previous article [24], but will be revisited in Section IV for Cases S3’ and  
 212 S4’ (this panel includes annotation of the interdune “flow channeling”, the importance of which will be revealed in  
 213 Section IV D). The discrete locations shown on Figure 2(b) ( $\mathbf{x}_L$ ,  $\mathbf{x}_C$ ,  $\mathbf{x}_E$ , and  $\mathbf{x}_F$ ) are used in Section IV C to record  
 214 time series of velocity and probability density functions (PDF; discussion to follow).

215 The dune DEMs were provided by Ken Christensen, Notre Dame, based on experimental work on turbulent flow  
 216 over barchan dunes in their refractive-index matched facility [11, 14]. The DEMs were, themselves, originally derived  
 217 from Hersen et al. [30]. Thus, attributes of the dunes have been carefully tuned to replicate natural morphological  
 218 states realized by actual dunes in nature.

## 219 IV. RESULTS

220 This section is composed of four subsections, which are used to systematically demonstrate how turbulence responds  
 221 to dunes and why the offset-merger interaction advances through the instantaneous realizations captured in Figure  
 222 1. The results will be used to demonstrate that asymmetry of the large, downflow dune is driven by a persistent  
 223 interdune roller. Vorticity dynamics reveal that sustenance of the roller is overwhelmingly derived from vortex  
 224 stretching mechanism: positive streamwise vorticity within the interdune space is supplied by hairpin vortices, which  
 225 are exposed to a channeling flow with positive streamwise velocity gradient.

### 226 A. Instantaneous and Reynolds-averaged flow: channeling and wake veering

227 Figure 3 shows instantaneous visualization of fluctuating streamwise-spanwise velocity (vectors) and swirl strength,  
 228 signed here by the unit vector for vorticity,  $\hat{\mathbf{i}}_\omega = \tilde{\omega}/|\tilde{\omega}| = \tilde{\omega}_x/|\tilde{\omega}|\hat{i} + \tilde{\omega}_y/|\tilde{\omega}|\hat{j} + \tilde{\omega}_z/|\tilde{\omega}|\hat{k}$  [56]. Thus, swirl strength is  
 229 a vector quantity,  $\boldsymbol{\lambda}_c^* = \lambda_c^*\hat{\mathbf{i}}_\omega$ . For the purpose of Figure 3, the color flood contour shows  $\lambda_{c,z}^*$ . Vortical activity is  
 230 concentrated within the wake regions of all dunes, where the local regions of  $\lambda_{c,z}^* > 0$  and  $\lambda_{c,z}^* < 0$  are indicators of  
 231 the legs of hairpins originating from the dune crests (additional results shown in Figure 5). In the interdune space  
 232 (i.e.,  $-3 \lesssim x/H \lesssim 1$  and  $0 \lesssim y/h \lesssim 2$  on Figure 3a), it is apparent that the small dune wake veers in conformance  
 233 with the large dune geometry. This is apparent also in Figure 3(b). In this article, we contend that wake veering from  
 234 the small dune is responsible for the large dune asymmetry.

235 Figure 4(a-f) shows contours of Reynolds-averaged vertical vorticity, where  $\langle \tilde{\omega}_z \rangle_t = \partial_x \langle \tilde{v} \rangle_t - \partial_y \langle \tilde{u} \rangle_t \approx -\partial_y \langle \tilde{u} \rangle_t$  since  
 236 the magnitude of spanwise heterogeneities must greatly exceed the magnitude of streamwise heterogeneities by virtue  
 237 of the wake shear [24]. Thus,  $\langle \tilde{\omega}_z \rangle_t$  is a marker of wake shear intensity. The contours reveal  $\langle \tilde{\omega}_z \rangle_t > 0$  and  $\langle \tilde{\omega}_z \rangle_t < 0$   
 238 in the wakes emanating from the “bottom” and “top” horns, respectively, where application of the right-hand rule  
 239 confirms the efficacy of this result. For completeness, we show the low-pass filtered wake centerline, found here via  
 240 location of points with  $\langle \tilde{\omega}_z \rangle_t(\mathbf{x}) = 0$  (where datapoints downflow of the small and large dune will be denoted with  
 241  $\delta_s(x_s; z)$  and  $\delta_l(x_l; z)$ , respectively, and where  $x_s$  and  $x_l$  are the origins of local coordinate systems; see Figure 2b).

242 For Case S1, the  $\langle \tilde{\omega}_z \rangle_t$  contours are roughly equal and opposite, and the wake centerline is virtually horizontal,  
 243 which is to be expected for an isolated obstacle. However, the addition of the spanwise-staggered small upflow dune

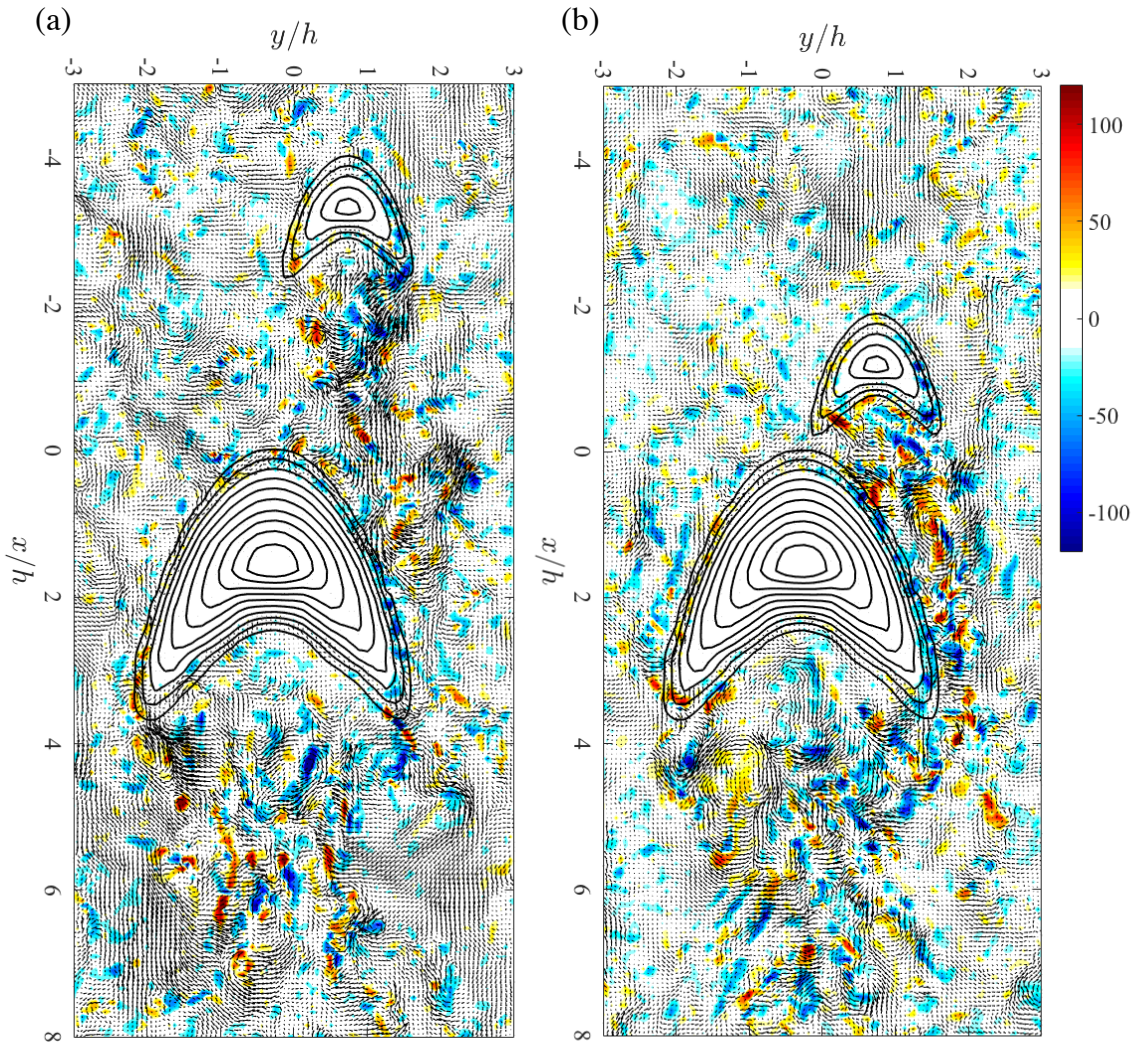


FIG. 3. Streamwise-spanwise plane visualization of instantaneous flow over Cases S5 (a) and S6 (b) (see Table I for topography details). Visualization shown at wall-normal elevation,  $z/h = 0.25$ . Contour and vectors are swirl strength with sign set by out-of-plane vorticity,  $\lambda_{c,z}^*(x, y, z/h = 0.25, t) = \lambda_c(x, y, z/h = 0.25, t)\hat{i}_{\omega,z}(x, y, z/h = 0.25, t)$ , and instantaneous fluctuating velocity,  $\{\tilde{u}'(x, y, z/h = 0.25, t)/u_*, \tilde{v}'(x, y, z/h = 0.25, t)/u_*\}$  respectively.

entirely disrupts this flow pattern. Indeed, for Case S2, the small dune wake veers through the interdune space, while the distribution of  $\langle \tilde{\omega}_z \rangle_t$  in the vicinity of the large dune is asymmetric. The zone of maximum  $|\langle \tilde{\omega}_z \rangle_t|$  on the “top” and “bottom” side of the large dune is rotated, where the negative (blue) and positive (red) zones have migrated upflow and downflow, respectively. In the interest of consistency, we adopted equivalent colorbar limits for the six panels, and we point out that the lower limit (negative) of the colorbar is roughly three times the magnitude of the upper limit (positive). The large negative values are concentrated on the “top” face of the downflow dune, and are developed as the flow is forced to channel through the interdune space. This result can be discerned, too, from inspection of the wake profiles, which even for Case S2 (maximum  $s_x/h$ , Figure 4h) exhibits a distinct veering, relative to Case S1.

As the spacing decreases for Cases S3 and S4 (Figure 4c,d), asymmetry in  $\langle \tilde{\omega}_z \rangle_t$  becomes more pronounced. Elevated  $|\langle \tilde{\omega}_z \rangle_t|$  across the large dune stoss face can be viewed as a proxy for surface stress, and the relatively larger values over the “top” region (i.e.,  $y/h > 0$  and  $x/h > 0$ ) are responsible for asymmetric morphology of the downflow dune (also observed in the flume experiments; Figure 1). At the elevation considered in Figure 4,  $z/h = 0.5$ , the small dune wake is far more sensitive to changing attributes of the topography, relative to the large dune. Recall, however, that the small dune height is equivalent to  $z/h = 0.5$ , and when the same contours are generated at  $z/h = 1$ , the large dune wake responds more to  $s_x/h$ , etc., but we have excluded these figures here for brevity.

For Cases S3' and S4' (Figures 4e,f), the small dune wakes are further perturbed, and yet the only difference

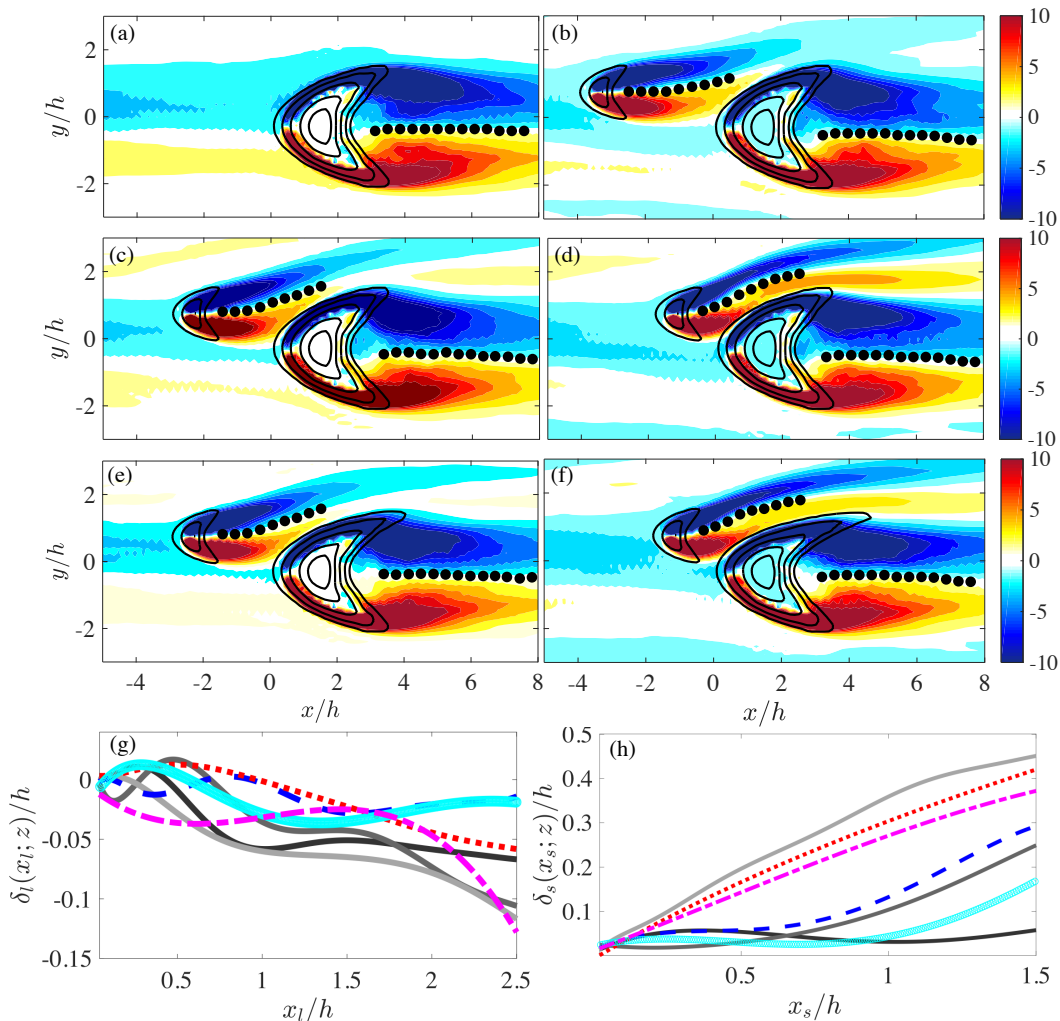


FIG. 4. Color flood contour of Reynolds-averaged vertical vorticity,  $\langle \tilde{\omega}_z \rangle_t(x, y, z/h = 0.5)$ , at wall-normal elevation,  $z/h = 0.5$ , for Cases S1 (a); S2 (b); S3 (c); S4 (d); S3' (e); and S4' (f) (see Table I for topography details). Included on the color floods are low-pass filtered datapoints for the wake, emanating from the small and large dunes,  $\delta_s(x_s; z/h = 0.5)$  and  $\delta_l(x_l; z/h = 0.5)$ , respectively. Low-pass filtered wake profiles emanating from large and small dunes,  $\delta_l(x_l; z/h = 0.5)$  (Panel g) and  $\delta_s(x_s; z/h = 0.5)$  (Panel h), respectively, where local coordinate originates at respective dune crest, where Figure 2 graphically illustrates the local axes,  $x_s$  and  $x_l$ . Black, gray, and light gray solid lines correspond with Cases S2, S3, and S4, respectively, dashed blue and dotted red lines correspond with S3' and S4', respectively, while cyan circles and dash-dot magenta line correspond with S5 and S6, respectively.

261 between these and Cases S3 and S4 is asymmetry of the large dune. Note, however, a subtle but important difference  
 262 in the  $\langle \tilde{\omega}_z \rangle_t$  distributions for Cases S3 and S3' (Figures 4c,e), and for Cases S4 and S4' (Figures 4d,f): for the “prime”  
 263 cases, the region of  $\langle \tilde{\omega}_z \rangle_t > 0$  (red) and  $\langle \tilde{\omega}_z \rangle_t < 0$  (blue) is larger and smaller, respectively. Since the small dune  
 264 forces elevated flow through the interdune space, the asymmetric dunes provide a larger area over which momentum  
 265 fluxes can occur (i.e., drag), and this helps to attenuate flow asymmetry.

266 We have recorded the wake profiles from Figure 4(a) to (f) and compiled them on Panels (g) and (h), which show  
 267  $\delta_s(x_s; z/h = 0.5)/h$  and  $\delta_l(x_l; z/h = 0.5)/h$ , respectively (see Figure 2 for graphical details of local coordinate system  
 268 and wake profiles). As per the caption, the black, gray, and light gray profiles correspond with Cases S2, S3, and S4,  
 269 respectively, and it is thus apparent that wake veering intensifies monotonically with decreasing  $s_x/h$  (this is true in  
 270 the wake of the small and large dune). Furthermore, comparing the wakes for S3 and S3' (gray and dashed blue),  
 271  $\delta_s(x_s; z)/h$  is similar between the two cases while  $\delta_l(x_l; z)/h$  is substantially smaller for the asymmetric dune. For  
 272 Cases S4 and S4' (light gray and dotted red),  $\delta_s(x_s; z)/h$  is, again, similar for the small dune but smaller for the  
 273 large asymmetric dune. This is attributed to the aforementioned weakening asymmetry in  $\langle \tilde{\omega}_z \rangle_t$  for Cases S3' and  
 274 S4', where the larger frontal area helps to absorb momentum on the face of the large dune exposed to the interdune

channeling flow. The cyan circles and dash-dot magenta line correspond with S5 and S6, respectively, and exhibit close agreement with the black and light gray profiles (S2 and S4). This serves as evidence of resolution insensitivity.

With the results presented in this section, we have established that asymmetry of the wakes is directly related to geometric attributes of the dunes. In the following section, we study the three-dimensional nature of flow processes proximal to the dunes using vortex identification and conditional sampling. We conditionally sample the flow based upon exceedence of a low-probability, high-magnitude event, which is especially relevant to aeolian systems since sediment mass fluxes scale nonlinearly upon ambient surface stress (which is set by turbulent fluctuations). Using wavelet decomposition, we will also demonstrate that vortices proximal to the dunes are a direct product of shedding from the dunes.

## B. Vortex shedding and wavelet analysis

This section addresses two complementary aspects of flow in the interdune space. Firstly, we present visualization of a vortex identifier derived from both the conditionally-averaged and instantaneous flow [57–61]. Since saltation mass fluxes are heavily influenced by intermittent fluctuations in imposed surface stress, it is important to consider flow attributes during extreme conditions [62–64]. This exercise confirms the existence of hairpin vortices being shed from the dune crests, which are forced to undergo downflow advection (in a subsequent section, we will demonstrate that streamwise vorticity originating within the hairpin legs is intrinsically important to large dune asymmetry). Given the importance of hairpin structures upon the morphodynamics, wavelet decomposition has been performed. The result confirms that the vortices are produced at a dominant frequency directly associated with the dune attributes.

Figure 2(c) shows Case S4' with annotations for discrete sampling locations,  $\mathbf{x}_L$ ,  $\mathbf{x}_C$ ,  $\mathbf{x}_F$ , and  $\mathbf{x}_E$  (see caption for additional information on discrete points). Flow statistics at these discrete locations are presumed to capture influences of the dune configurations. Here, we focus specifically on position  $\mathbf{x}_L/h = \{1.0, 0.5, 0.5\}$ , at which the influence of flow channeling, separation from the small dune, and changing dune topographic configurations, are especially pronounced.

Time-series recording of  $\tilde{u}'(\mathbf{x}_L, t)/u_*$ , over  $\sim \mathcal{O}(10^3)$  large-eddy turnovers have been used to generate the PDF shown in Figure 5(a, inset). The PDFs exhibit wide, or heavy, tails that are the signature of intermittent, high-magnitude events. Moreover, the PDFs contain rich information about how upflow disturbances due to the relatively smaller dune can profoundly alter the statistics at downflow points. Since the mean flow has been subtracted before generating the PDFs, the PDFs are all centered around 0 (this facilitates intercomparison between the cases). Firstly, the PDFs exhibit clear widening for Cases S1 to S4, which is due to the diminishing  $s_x/h$ , for which the wake effects due to the small dune are closer to the sampling point. Note, too, that the PDFs for Cases S3' (dashed blue) and S4' (dotted red) exhibit yet wider PDFs, and, thus, the probability of the mean is least for these cases.

For discussion, consider the existence of a site at which the prevailing winds can not develop a Reynolds-averaged  $u_*$  capable of exceeding the threshold needed to mobilize sediment,  $u_{*,t}$  [1, 19–21] (in the context of aeolian processes on Earth, such conditions could occur due to seasonal meteorological variability). However, the PDFs in Figure 5(a) show that  $u_*$  – which is set by fluctuations in the aloft flow – could greatly exceed its average over brief periods of time. In a related article, Chinthaka and Anderson [64] recently used LES to reveal the spatial attributes of flow structures in the atmospheric boundary layer during brief, high-magnitude values of  $u_*$ , and showed how coherent structures within the atmospheric surface layer could induce stresses substantially exceeding the average.

For the present article, we used the threshold,  $\tilde{u}'(\mathbf{x}_L, t)/u_* > 2.5$ , which has been added as an annotation on Figure 5(a, inset). Since the PDFs all exhibit different distributions, the resultant conditionally-averaged statistics do not correspond with an event likely to occur with the same probability. It is apparent, however, that in all cases we have sampled the flow based on events with a 5 to 15 % probability of occurrence.

After computation of the PDF and selection of the threshold, we then run the LES for an additional period of time and sample the flow based on:

$$\frac{\widehat{\mathbf{u}}(\mathbf{x})}{u_*} = \left\langle \frac{\tilde{\mathbf{u}}(\mathbf{x}, t)}{u_*} \middle| \frac{\tilde{u}'(\mathbf{x}_L, t)}{u_*} > 2.5 \right\rangle_{N_s}, \quad (3)$$

where  $\widehat{\cdot}$  denotes a conditionally-averaged quantity, and  $N_s$  is the number of times  $\tilde{u}'(\mathbf{x}_L, t)/u_* > 2.5$ . Having conditionally sampled the flow with Equation 3, we compute the  $Q$  criterion vortex identifier, which is derived from the velocity gradient tensor,  $\mathbf{D} = \nabla \tilde{\mathbf{u}}$  [65–67].  $\mathbf{D}$  can be decomposed into its symmetric and anti-symmetric components,  $\mathbf{D} = \mathbf{S} + \mathbf{\Omega}$ , where  $\mathbf{S} = \frac{1}{2} (\nabla \tilde{\mathbf{u}} + \nabla \tilde{\mathbf{u}}^T)$  and  $\mathbf{\Omega} = \frac{1}{2} (\nabla \tilde{\mathbf{u}} - \nabla \tilde{\mathbf{u}}^T)$ , allowing computation of the  $Q$  criterion with:

$$Q = \frac{1}{2} (\mathbf{\Omega} : \mathbf{\Omega} - \mathbf{S} : \mathbf{S}). \quad (4)$$

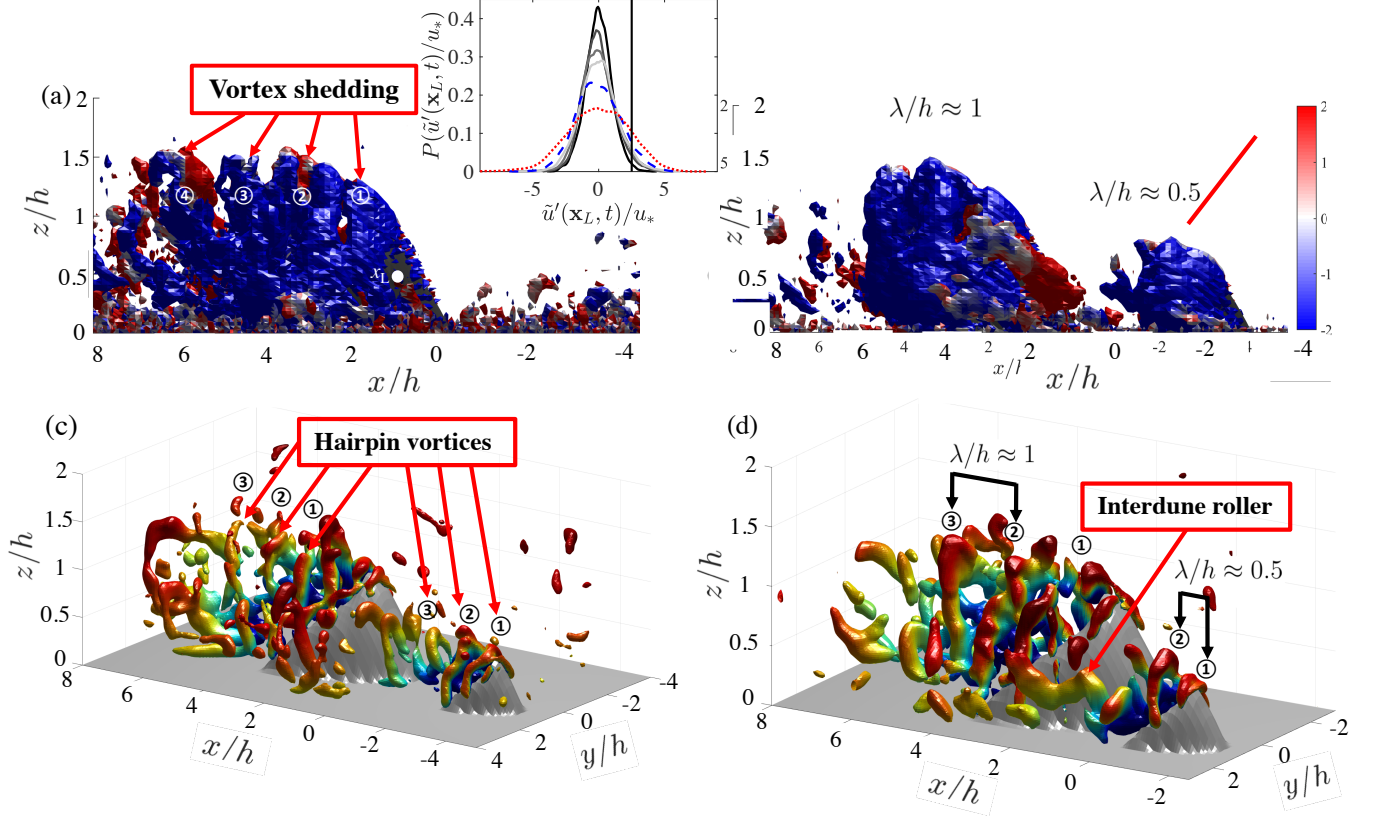


FIG. 5. Streamwise–wall-normal visualization of conditionally-averaged  $Q$  criterion for  $\widehat{Q}=11$  signed by conditionally-averaged wall-normal rotating direction: Panels (a) and (b) show Cases S1 and S2, respectively. Probability density function (PDF) of normalized streamwise velocity fluctuation at sampling position  $\mathbf{x} = \mathbf{x}_L$  is showed in panel (a). Black, dark gray, gray, and light gray lines correspond with Cases S1, S2, S3, and S4, respectively, while dashed blue and dotted red datapoints correspond with S3' and S4', respectively (see Table I and Figure 2 for topography details). Black vertical line notes the conditional sampling threshold used in this work is  $\tilde{u}'(\mathbf{x}_L, t)/u_* > 2.5$  [57–64]. Three dimensional visualization of instantaneous  $Q$  criterion for  $Q=100$  signed by Reynolds-averaged streamwise velocity: Panels (c) and (d) show Cases S5 and S6, respectively. Note numbered annotation of successive vortex cores emanating from dune brinkline, and vortex core spacing,  $\delta_s/h$ , deduced from high-Reynolds number Strouhal number and advective velocity in vicinity of brinkline.

326 Figures 5(a) and 5(b) show isosurfaces of conditionally-averaged  $Q$  criterion for Cases S1 and S2, respectively,  
 327 in the streamwise–wall-normal plane (see Figure 5a-inset for conditional sampling threshold). These figures reveal  
 328 the presence of a train of vortex cores, migrating downflow following separation at the crest (for Case S1, we have  
 329 annotated vortex cores 1 to 4, while for Case S2, we have annotated vortex cores in the wake of the large and  
 330 dune). Figures 5(c) and 5(d) show three-dimensional isosurfaces of instantaneous  $Q$  criterion for high-resolution  
 331 cases, S5 and S6, respectively. Compared with the conditionally-averaged visualizations, instantaneously-sampled  
 332 three-dimensional fields from the high-resolution cases are relatively less organized. Nonetheless, there is a discernible  
 333 pattern of hairpin-like structures emanating downflow of both dunes, while one of the cases has captured the interdune  
 334 roller (Panel d). The interdune roller, we will show, is foremost in setting the asymmetric topology of the larger dune.  
 335 The structure of successive hairpin heads resembles observations from canonical wall turbulence [67, 68].

336 To explain the downflow spacing between successive vortex cores annotated in Figure 5, we have used global wavelet  
 337 power spectrum. Wavelet decomposition is a convenient tool for illustrating the spectral density of input time series  
 338 in joint time-frequency space [69, 70]. Global wavelet power spectrum profiles are attained via convolution of an  
 339 input time series with a spectrum of wavelet functions, computation of spectral density (wavelet power spectrum  
 340 contour), and averaging over time at each distinct frequency (global wavelet power spectrum profile). This procedure  
 341 is useful in the detection of energetic peaks associated with vortex shedding downflow of the large dune. For the  
 342 present analysis, we consider  $\tilde{u}(\mathbf{x}_L, t)$  and  $\tilde{u}(\mathbf{x}_C, t)$ , discrete locations roughly upflow and downflow of the large dune,  
 343 respectively (see Figure 2c). The analysis is predicated upon convolution of  $\tilde{u}'(\mathbf{x}, t)$  with a wavelet (basis) function,

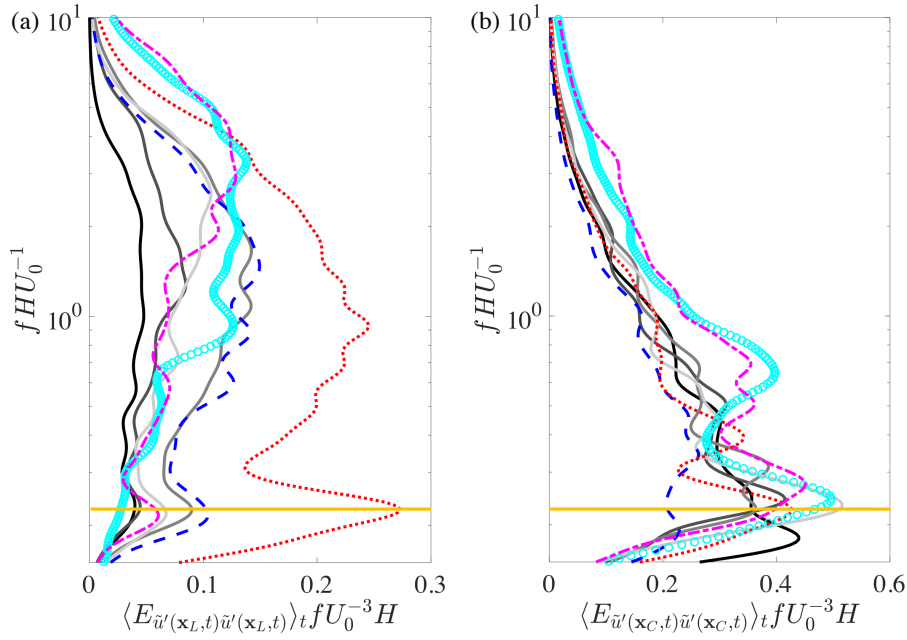


FIG. 6. Global wavelet power spectrum of streamwise velocity fluctuations, for input time series from discrete locations  $\mathbf{x}_L$  (a) and  $\mathbf{x}_C$  (b). Black, dark gray, gray, and light gray lines correspond with Cases S1, S2, S3, and S4, respectively, dashed blue and dotted red lines correspond with S3' and S4', respectively, while cyan circles and dash-dot magenta line correspond with S5 and S6, respectively. Horizontal orange line denotes  $fHU_0^{-1} = St = 0.25$ , the high-Reynolds number asymptote.

344  $\psi(f)$ , which yields an array of coefficients in joint time-frequency space. The square of the absolute value of the wavelet  
 345 coefficients, divided by each frequency, yields spectral density defined in time-frequency space,  $E_{\tilde{u}'\tilde{u}'}(\mathbf{x}, t)fU_0^{-3}H$ ,  
 346 otherwise known as wavelet power spectrum contours. For the present work, we have used Morlet wavelets,  $\psi(t/t_s) =$   
 347  $\exp(i\omega_\psi t/t_s) \exp(-|t/t_s|^{2\frac{1}{2}})$ , where we have chosen the relatively common non-dimensional frequency,  $|\omega_\psi| = 6$ , for  
 348 which  $t_s$  is the wavelet timescale,  $t$  is physical time, and  $i$  is the imaginary unit.

349 Figure 6 shows global wavelet power spectrum profiles for the input time series denoted in the figure caption,  
 350  $\langle E_{\tilde{u}'\tilde{u}'}(\mathbf{x}, t) \rangle_t fU_0^{-3}H$ . Frequency has been shear normalized for the present purposes, where the ordinate label is  
 351 equivalent to Strouhal number,  $St = fHU_0^{-1}$ , where  $U_0$  is Reynolds-averaged streamwise outer velocity (i.e.,  $U_0 =$   
 352  $\langle \tilde{u}(x, y, z/H = 1, t) \rangle_{x, y, t}$ ). For high-Reynolds number flows, such as the present, Strouhal number tends toward an  
 353 asymptotic value,  $St \approx 0.25$ , which has been denoted by the horizontal orange line on Figure 6. For Case S1 at  
 354 location  $\mathbf{x}_L$ , there is no distinct peak in any component of velocity. Instead, energy is distributed across constituent  
 355 frequencies, due to the presence of channel-like turbulence upflow of the large dune (centered around a peak at  
 356  $fHU_0^{-1} \approx 1$ , a characteristic large-eddy timescale). However, the addition of the smaller upflow dune changes the  
 357 spectral densities significantly.

358 Indeed, at position  $\mathbf{x}_L$ , the spectral densities of streamwise velocity fluctuation reveal the emergence of a second  
 359 peak at  $fHU_0^{-1} \approx 0.25$ , which is the marker of vortex shedding from the upflow dune. As the streamwise spacing  
 360 decreases, the energy associated with vortex shedding increases, and this is true for all cases. In contrast, at position  
 361  $\mathbf{x}_C$ , all input time series are affected by vortex shedding (including Case S1). Figure 6(b) reveals that the vortex  
 362 shedding peak is the dominant energy-containing frequency, and visual inspection of Figure 2 shows this to be a logical  
 363 result given the proximity of  $\mathbf{x}_C$  to the crest of the large dune. Note, too, that the profiles for Cases S2 and S4 are  
 364 similar (profile and magnitude) to the profiles for S5 and S6, respectively, providing further evidence of resolution  
 365 insensitivity in the LES code (color coding summarized in the figure caption).

366 Since Figure 6 has revealed a distinct energetic peak associated with vortex shedding at  $St = fHU_0^{-1} = 0.25$ ,  
 367 we can return now to Figure 5 and the streamwise spacing between successive vortex cores. For the purposes of an  
 368 estimation, we presume that the advective velocity of each vortex core is  $U_0$ , which can be related to the distance  
 369 between successive hairpin vortices,  $\lambda$ , via  $U_0 = \lambda f$ . With this,  $U_0 = \lambda St U_0 / H$ , which can be rearranged to  $\lambda = St H$ .  
 370 Put differently, we can normalize by the dune height, yielding  $\lambda/h \approx 1$  and  $\lambda/h \approx \frac{1}{2}$  for the large and small dune,  
 371 respectively. Annotations for this spacing have been added to Figure 5. Inspection of Figure 5 shows that this exercise  
 372 yields perfectly consistent predictions on the vortex core spacing, and confirms that vortical activity proximal to the  
 373 dunes originates via separation from the dune crests.

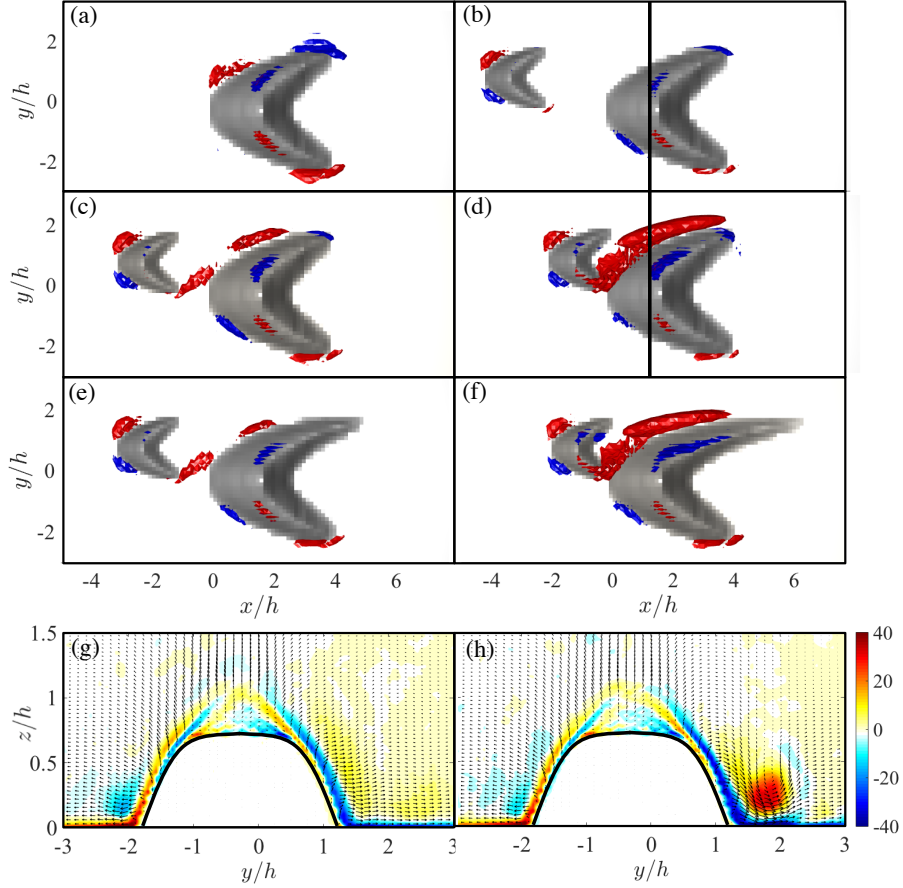


FIG. 7. Isosurface image of Reynolds-averaged, shear-normalized differential helicity,  $h(\mathbf{x})Hu_*^{-2} = 120$  (red) and  $h(\mathbf{x})Hu_*^{-2} = -120$  (blue). Panels (a) to (f) correspond with Cases S1, S2, S3, S4, S3' and S4', respectively. Panel (g) and (h) are Reynolds-averaged flow over S5 (g) and S6 (h) in spanwise-wall normal plane at  $x/h = 1.7$ , which are showed as black lines in panel (b) and (d) respectively (see Figure 2 for reference). In (g) and (h), contour and vectors are Reynolds-averaged streamwise vorticity,  $\langle \tilde{\omega}_x(\mathbf{x}) \rangle_t$ , and components of in-plane velocity,  $\{ \langle \tilde{v}(\mathbf{x}, t) \rangle_t, \langle \tilde{w}(\mathbf{x}, t) \rangle_t \}$ .

374

### C. Sediment scour and asymmetric erosion

In this Section, we will further elaborate on the significance of the interdune roller in the context of dune morphodynamics. Firstly, we will illustrate the existence of the interdune roller through introduction of differential helicity – a quantity that defaults to zero in the absence of simultaneous, co-aligned velocity and vorticity. In the present context, helicity is ideal for studying the interdune roller since its presence highlights both the channeling flow and streamwise vorticity. We will conclude that this constitutes a “channel-and-scour” mechanism, and show that this mechanism explains the pronounced asymmetry of the large dune during offset interaction (Figure 2). With this, a structural model is presented to summarize how hairpins shed from the upflow dune introduce streamwise vorticity, and how this streamwise vorticity drives asymmetric erosion across the large dune.

Reynolds-averaged, differential helicity is computed as the inner product of velocity and vorticity:

$$H_l = \int \langle \tilde{\omega}(\mathbf{x}, t) \cdot \tilde{\mathbf{u}}(\mathbf{x}, t) \rangle_t d^3\mathbf{x}, \quad (5)$$

where  $d^3\mathbf{x}$  is the volume over which  $H_l$  is to be computed. For the present purposes, it is more convenient to consider differential helicity,

$$h_l(\mathbf{x}) = \frac{dH_l}{d^3\mathbf{x}} = \langle \tilde{\omega}(\mathbf{x}, t) \cdot \tilde{\mathbf{u}}(\mathbf{x}, t) \rangle_t. \quad (6)$$

In the absence of coalignment between the velocity and vorticity vectors, helicity vanishes. In the context of the interdune roller, differential helicity (as per Equation 6) is interesting since it reveals the presence of any accompanying

389

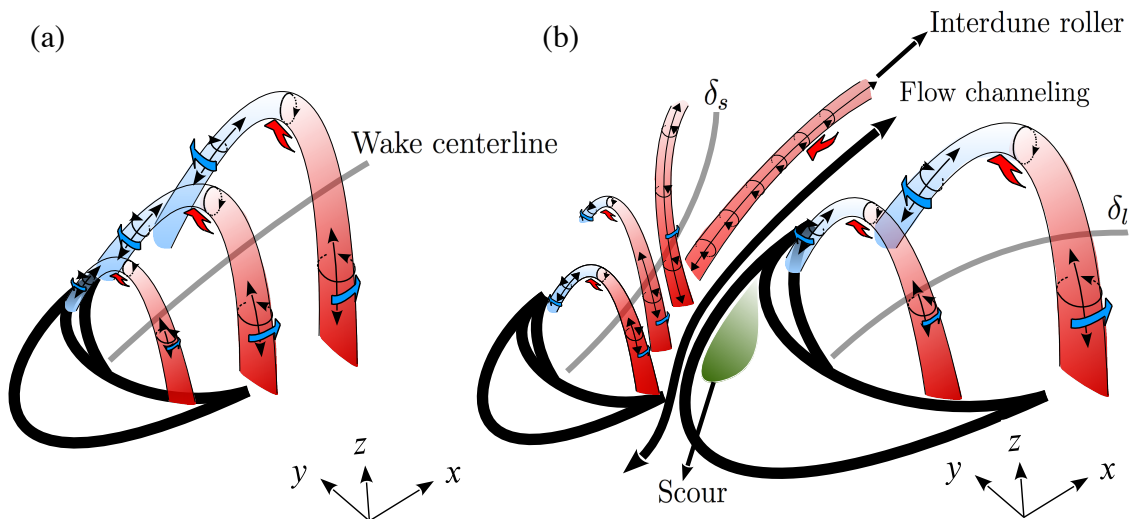


FIG. 8. Structural model for flow processes associated with dune morphodynamic asymmetry. Panel (a): idealized hairpin vortices shed from dune brinkline; Panel (b): idealized hairpin vortices being simultaneously shed from both dunes, where streamwise vorticity embodied within inner leg of upflow hairpin is stretched by flow channeling (double-headed roller), sustaining the interdune roller and inducing sediment scour on the large dune (green). Red and blue colors denote positive and negative streamwise vorticity directions, respectively (see Figure 5c,d for three-dimensional instantaneous visualization). On both panels, gray lines denote dune wake centerline (see also Figures 2 and 4 for details).

390 advection. This is relevant to dune morphodynamics, since it implies that the interdune roller scours sediment from  
 391 the large dune while simultaneously inducing net downflow transport. Figure 7(a-f) shows isosurfaces of  $h_l(\mathbf{x})$ , as per  
 392 Equation 6.

393 It is apparent, firstly, that the  $h_l(\mathbf{x})$  distribution is roughly symmetric for Case S1 (Figure 7a). However, even  
 394 for Case S2 (largest  $s_x/h$ ), the  $h_l(\mathbf{x})$  distribution is entirely modified. As the upflow dune approaches the larger  
 395 downflow dune (Cases S3 and S4, Figure 5c,d), the spatial extent of the advecting interdune roller increases. The  
 396  $h_l(\mathbf{x})$  isosurface is actually smaller for Cases S3' and S4', which is consistent with preceding results on attenuation of  
 397 flow asymmetry (i.e., Figures 6 and 8) for the asymmetric dune cases. We clarify, finally, that streamwise vorticity and  
 398 velocity make the dominant contribution to helicity, i.e.,  $h_l(\mathbf{x}) \approx \tilde{\omega}_x(\mathbf{x})\tilde{u}(\mathbf{x})$ . Thus, the isosurfaces are true markers  
 399 of a roller undergoing persistent advection through the interdune space.

400 In order to demonstrate the importance of the interdune roller for sediment scour from the large dune, and thus  
 401 morphodynamic asymmetry, Figure 7(g,h) shows spanwise-wall-normal visualization of Reynolds-averaged streamwise  
 402 vorticity for Cases S5 (Panel g) and S6 (Panel h), where the  $y-z$  plane positions have been denoted as solid black lines  
 403 on Figure 7(b,d), respectively. The signature of the interdune roller is captured in the red region of  $\langle \tilde{\omega}_x(\mathbf{x}) \rangle_t$ ,  
 404 while the vector field shows how the roller induces scour down the face of the large dune (while channeling through the  
 405 interdune space transports sediment downflow, advancing the interaction and enforcing morphodynamic asymmetry).

406 For completeness, Figure 8 is an idealized sketch of these process for an isolated (Panel a) and offset interaction  
 407 (Panel b) configuration. For the isolated case, we have sketched production of a succession of idealized hairpins  
 408 [7, 9, 10, 12, 13, 71], which migrate downflow (supporting instantaneous and quantitative supporting results of this  
 409 were reviewed in Section IV B). For the offset interaction case, however, the picture changes significantly. Here, self-  
 410 similar hairpins are produced via separation at the small dune crest. The hairpins are colored by streamwise vorticity,  
 411 which explains how separation from the small dune serves as the source of streamwise vorticity. Upon production,  
 412 this streamwise vorticity is subjected to immediate stretching due to the channeling flow (this section). As a result, a  
 413 persistent interdune roller is present in the interdune space – confirmed, also, with visualization of differential helicity  
 414 – and this roller scours sediment from the inner face of the large dune (Figure 8b). Sediment eroded by the roller  
 415 is transported downflow before being deposited, which explains the asymmetry exhibited by the large dune as the  
 416 interaction proceeds. The sketch also provides annotations of the wake veering profiles, which were reviewed in Section  
 417 IV A.

418 The results in this section have highlighted the simultaneous importance of the interdune channeling flow and its  
 419 rotational sign. We argue that the interdune roller scours sediment from the large dune, and that this is foremost in  
 420 setting the dune morphology as interaction advances. In order to close the argument, we present results of vorticity  
 421 budgeting in the following section. Results demonstrate that, indeed, stretching of ambient streamwise vorticity

422 provides the largest gain to streamwise vorticity in the interdune space.

### 423 D. Turbulent vorticity dynamics

424 As a final post-processing measure, we have used the Reynolds-averaged velocity and total stresses to elucidate  
425 mechanisms responsible for sustaining the interdune roller. Consider, first, the Reynolds-averaged incompressible  
426 momentum transport equation:

$$427 \quad \frac{1}{2} \nabla \cdot (\langle \tilde{\mathbf{u}} \rangle_t \cdot \langle \tilde{\mathbf{u}} \rangle_t) - \langle \tilde{\mathbf{u}} \rangle_t \times \langle \tilde{\boldsymbol{\omega}} \rangle_t = -\frac{1}{\rho} \nabla \tilde{p} - \nabla \cdot \langle \mathbf{T} \rangle_t + \mathbf{\Pi} + \mathbf{f}, \quad (7)$$

428 where  $\mathbf{T} = \langle \mathbf{u}' \otimes \mathbf{u}' \rangle_t = \langle \tilde{\mathbf{u}}' \otimes \tilde{\mathbf{u}}' \rangle_t + \langle \boldsymbol{\tau} \rangle_t$ , where the first and second right-hand side terms are the resolved and  
429 subgrid-scale stress tensor (this additive approach is necessary when assembling the total stresses from LES datasets  
430 *a posteriori*);  $\mathbf{f}$  represents imposed forces associated with the presence of solid obstacles via an IBM (see also Section  
431 II), while  $\mathbf{\Pi}$  denotes any ambient pressure-gradient forcing. The transport equation for  $\langle \tilde{\boldsymbol{\omega}} \rangle_t$  is derived via the curl of  
432 Equation 7, yielding:

$$433 \quad \underbrace{\langle \tilde{\mathbf{u}} \rangle_t \cdot \nabla \langle \tilde{\boldsymbol{\omega}} \rangle_t}_{\text{Advection}} = \underbrace{\langle \tilde{\boldsymbol{\omega}} \rangle_t \cdot \nabla \langle \tilde{\mathbf{u}} \rangle_t}_{\text{Stretching and Tilting}} - \underbrace{\nabla \times \nabla \cdot \langle \mathbf{T} \rangle_t}_{\text{Turbulent torque}}, \quad (8)$$

434 where annotations have been used to denote the stretching and tilting of  $\langle \tilde{\boldsymbol{\omega}} \rangle_t$  via mean-flow gradients, and gains/losses  
435 to  $\langle \tilde{\boldsymbol{\omega}} \rangle_t$  via spatial heterogeneity of  $\mathbf{T}$  (so called turbulent torque). The former and latter are also referred to as  
436 Prandtl's secondary flow of the first and second kind [72, 73], respectively. The analysis from Section IV A to IV C  
437 demonstrates that: (a) there is flow channeling within the interdune space; and: (b) this channeling flow stretches  
438 hairpin vortices downwind, enabling gains in streamwise vorticity. Thus, in this section, we will consider only the  $x$   
439 component of Equation 8:

$$440 \quad \underbrace{\langle \tilde{\mathbf{u}} \rangle_t \cdot \nabla \langle \tilde{\omega}_x \rangle_t}_{\text{Advection}} = \underbrace{\langle \tilde{\omega}_x \rangle_t \partial_x \langle \tilde{u} \rangle_t}_{\text{Stretching, } \langle S_x(\mathbf{x}) \rangle_t} + \underbrace{\langle \tilde{\omega}_y \rangle_t \partial_y \langle \tilde{u} \rangle_t + \langle \tilde{\omega}_z \rangle_t \partial_z \langle \tilde{u} \rangle_t}_{\text{Tilting, } \langle T_x(\mathbf{x}) \rangle_t} - \underbrace{\epsilon_{xqi} \partial_q \partial_j \langle T_{ij} \rangle_t}_{\text{Turbulent torque, } \langle P_x(\mathbf{x}) \rangle_t}. \quad (9)$$

441 The symbolic annotations beneath each term in Equation 9 will be used later to explain mechanisms driving gains  
442 and losses to  $\langle \tilde{\omega}_x \rangle_t$ . It is apparent, from inspection, that the first right-hand side term corresponds with stretching  
443 of  $\langle \tilde{\omega}_x \rangle_t$ , while the second right-hand side term corresponds with tilting of  $\langle \tilde{\omega}_y \rangle_t$  and  $\langle \tilde{\omega}_z \rangle_t$  into the  $x$  direction (note  
444 that the sum of these terms was referred to as  $\langle P_x(\mathbf{x}) \rangle_t$  by Perkins [72]).

445 In Figure 9, we show vertical profiles of the stretching, tilting, and turbulent torque terms in Equation 9, at discrete  
446 locations  $\mathbf{x}_E$  and  $\mathbf{x}_F$ , respectively. As shown in Figure 2,  $\mathbf{x}_E$  and  $\mathbf{x}_F$  are at equal streamwise positions, but from  
447 outside and within the interdune space, respectively. Thus, differences in the profiles of constituent terms in Equation  
448 9 at these locations can be attributed to asymmetries associated with the channeling flow, etc. At location  $\mathbf{x}_E$ ,  
449 Figure 9(a-c) shows that the profiles for different dune configurations do not exhibit dramatic differences, even as  
450 the geometry changes. We see, too, that turbulent torque (Panel c) makes the dominant contribution to gains and  
451 losses in Reynolds-averaged streamwise vorticity. Vortex stretching (a) and tilting (b) makes a relatively modest  
452 contribution, relative to turbulent torque. At location  $\mathbf{x}_F$ , however, the picture changes dramatically, in order to  
453 sustain the interdune roller and channeling flow.

454 Figure 9(d-f) shows the right-hand side terms of Equation 9, at location  $\mathbf{x}_F$ . It is clear, now, that the upflow dune  
455 entirely changes flow processes in the interdune space. Relative to  $\mathbf{x}_E$ , the magnitudes of constituent terms are all  
456 higher. It is clear, too, that the largest contribution is derived from the stretching term (Panel d). The peak occurs  
457 around  $z/h = 0.25$  for Case S4 (light gray) and Case S4' (dotted red line), which is the signature of flow channeling  
458 (stretching) of streamwise vorticity. The magnitude of turbulent torque at  $\mathbf{x}_F$  exceeds the values reported at  $\mathbf{x}_E$ , but  
459 is still small relative to the contribution from stretching.

460 Figure 9 was used to conclude that stretching provides the largest gain to sustenance of the interdune roller,  
461 although this argument was predicated only upon a profile from a discrete location. To further the argument, we have  
462 prepared Figure 10: a horizontal contour of the stretching term, with the wake profiles from Figure 4 superimposed  
463 for generality. For the isolated case (Panel a), the magnitude of the stretching term is equal and opposite on the dune  
464 stoss face, and the wake exhibits no veering. With introduction of the upflow dune, however, an additional location  
465 of stretching is introduced (Panel b to f), and the magnitude of this grows monotonically as spacing decreases (Panels  
466 b to d).

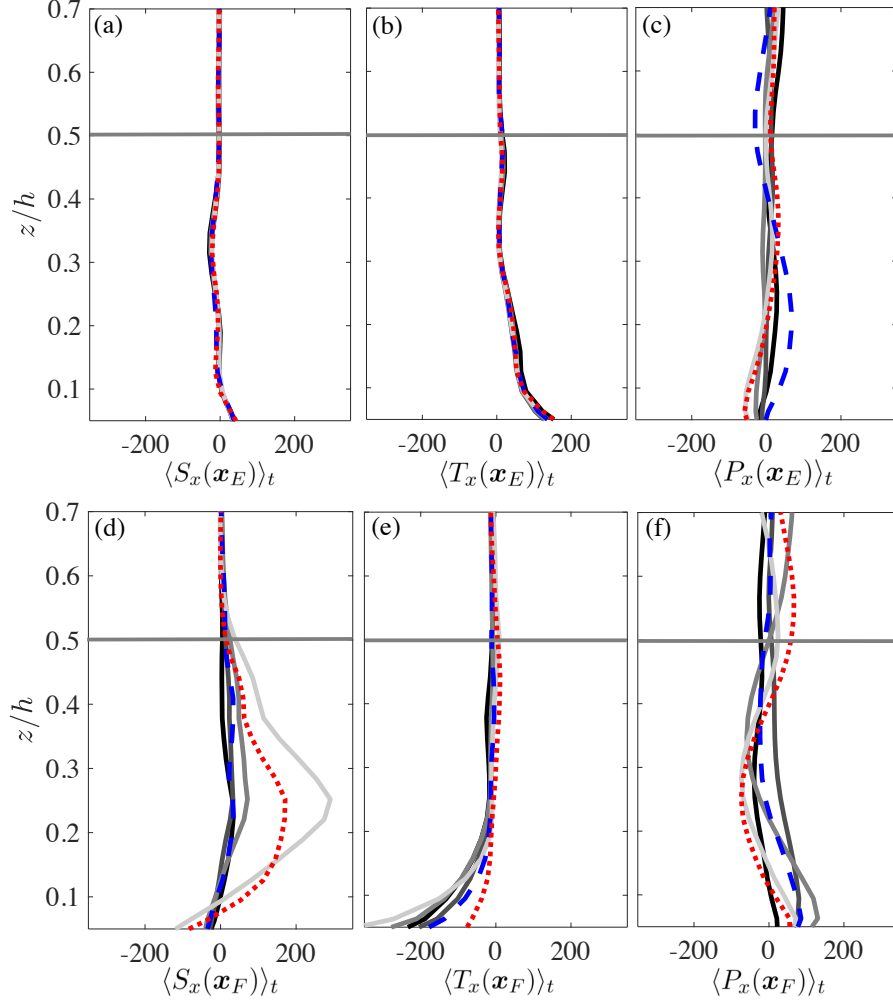


FIG. 9. Vertical profiles of constituent right-hand side terms from Reynolds-averaged streamwise vorticity transport Equation (Equation 9), including vortex stretching  $\langle S_x \rangle_t$  (a,d), vortex tilting  $\langle T_x \rangle_t$  (b,e) and turbulent torque  $\langle P_x \rangle_t$  (c,f) at discrete streamwise-spanwise locations collocated with Point  $\mathbf{x}_E$  (a, b ,c) and Point  $\mathbf{x}_F$  (d, e, f) (see also Figure 2). Black, dark gray, gray, and light gray lines correspond with Cases S1, S2, S3, and S4, respectively, while dashed blue and dotted red lines correspond with S3' and S4', respectively. Horizontal gray line denotes small dune height.

## V. CONCLUSION

467

468 For this work, we used LES to model turbulent high-Reynolds number flow over a series of dune field configurations.  
 469 The configurations were selected to capture instantaneous realizations of the so-called offset merger interaction,  
 470 wherein a smaller upflow dune approaches a larger downflow dune. Flume observations have revealed that during  
 471 advancement of this interaction, the large dune morphology develops a pronounced asymmetry: the horn that is  
 472 streamwise aligned with the path of the upflow dune exhibits a relatively larger downflow elongation (Figure 1). In  
 473 order to capture the aero-/hydro-dynamic processes responsible for this interaction, two of the configurations featured  
 474 downflow dunes with significant asymmetry (S3' and S4').

475 We showed how the wake profiles of the individual dunes varies with spatial attributes of the configuration, and we  
 476 showed that the extent of Reynolds-averaged flow asymmetry *declines* for cases in which the large dune is asymmetric.  
 477 Since the asymmetric dunes feature a larger surface area over which momentum fluxes (drag) can occur, the asymmetry  
 478 serves to attenuate large mean-flow gradients in the interdune space.

479  $Q$  criterion was used to highlight the vortical nature of flow around the dunes, which demonstrated the presence of a  
 480 persistent interdune roller. Shedding of hairpin vortices was ostensible in the conditionally-averaged and instantaneous  
 481 flow. We showed that the dunes impart a distinct energetic peak in the global wavelet power spectrum, accomplished  
 482 by convolving the input time series of streamwise velocity fluctuations with a spectrum of wavelet functions, and we

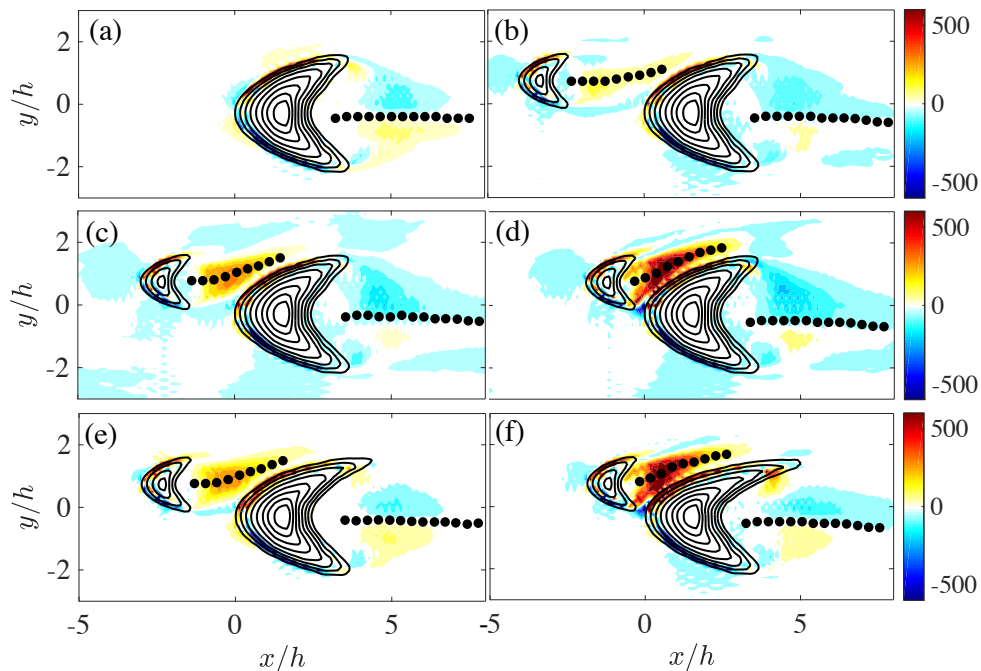


FIG. 10. Color flood contour of Reynolds-averaged term responsible for stretching of streamwise vorticity,  $\langle S_x \rangle_t(x, y, z/h = 0.25)$  (see also Equation 9). Panels (a) to (f) correspond with Cases S1, S2, S3, S4, S3' and S4', respectively. Included on the color floods are low-pass filtered datapoints for the wake, emanating from the small and large dunes,  $\delta_s(x_s; z/h = 0.25)$  and  $\delta_l(x_l; z/h = 0.25)$ , respectively.

483 related this to the high-Reynolds number Strouhal number. This result was used to provide a cursory estimate for the  
 484 streamwise spacing between successive rollers, which agreed well with visualizations of vortex cores emanating from  
 485 the dune crests.

486 To reconcile preceding findings, we showed contours of differential helicity, since the absence of helicity would  
 487 indicate an “in place” roller. However, the silhouette of helicity isosurfaces were virtually identical to those of  $Q$   
 488 criterion, demonstrating that the interdune roller is undergoing persistent migration through the interdune space.  
 489 This result confirmed, then, that erosion of the large dune is driven by two complementary mechanisms: (1) the  
 490 interdune roller scours sediment laterally from the large dune; and (2) channeling flow drives saltating grains through  
 491 the interdune space, with saltation mass flux declining as the interdune channeling flow attenuates.

492 Given the morphodynamic importance of the interdune roller, we performed a detailed vorticity dynamics analysis  
 493 to elucidate terms responsible for its sustenance. At these very high Reynolds numbers, vorticity gains and losses occur  
 494 in response to the stretching and tilting effects, and via spatial heterogeneity of the Reynolds stresses. We considered  
 495 terms responsible for sustenance of streamwise vorticity, since the roller was closely aligned with this direction. The  
 496 results show that stretching makes the largest contribution to sustenance of the roller, which is thoroughly consistent  
 497 with arguments throughout the article on the importance of the interdune roller. A structural model to summarize  
 498 this process was presented.

499 Results herein suggest that coherent flow structures within the interdune space – critical to the spatial distributions  
 500 of basal stress, but entirely neglected by existing flow descriptions based only on surface slope [65, 74] – are important  
 501 in shaping the spatial complexity of natural dunes. Indeed, the results show that the dunes themselves induce  
 502 flow patterns that sustain flow structures, confounding slope-based descriptions. The application considered herein,  
 503 the offset-merger interaction, was selected for its convenience and due to prior flume work, although the results have  
 504 conceptual transcendence to other dune interactions: that is, the flow patterns associated with each dune are persistent  
 505 over very large distances, and the interaction between such flow patterns can produce non-obvious structures (i.e.,  
 506 the interdune roller, as is the case for the offset-interaction merger).

## ACKNOWLEDGMENTS

507

508 This work was supported by the National Science Foundation, Grant # CBET-1603254. Scientific computing  
 509 resources were provided by the Texas Advanced Computing Center at the University of Texas at Austin. We thank  
 510 Kalyan Shrestha, UT Dallas, for generously sharing a MatLab visualization script used to create three-dimensional  
 511 isosurfaces of flow quantities. We thank Ken Christensen, Notre Dame, for providing the barchan dune DEMs used  
 512 to create the dune configurations considered for this work.

- 
- 513 [1] R. Bagnold, *The Physics of Blown Sand and Desert Dunes* (Chapman and Hall, 1956).  
 514 [2] I. Livingstone, G. Wiggs, and C. Weaver, *Earth-Science Review* **80**, 239 (2006).  
 515 [3] A. Frank and G. Kocurek, *Geomorphology* **17**, 47 (1996).  
 516 [4] J. Best, *J. Geophys. Res.* **110**, F04S02, doi:10.1029/2004JF000218 (2005).  
 517 [5] J. Best, *Fluvial Sedimentology VII* **35**, 41 (2005).  
 518 [6] J. Fröhlich, C. Mellen, W. Rodi, L. Temmerman, and M. Leschziner, *J. Fluid Mech.* **526**, 19 (2005).  
 519 [7] T. Stoesser, C. Braun, M. Garcia-Villalba, and W. Rodi, *J. Hydr. Eng.* **134**, 42 (2008).  
 520 [8] Y. Shao, *Physics and Modelling of Wind Erosion* (Springer Verlag, 2008) p. 452pp.  
 521 [9] M. Omidyeganeh and U. Piomelli, *J. Turbulence* **12**, 1 (2011).  
 522 [10] M. Omidyeganeh and U. Piomelli, *J. Fluid Mech.* **721**, 454 (2013).  
 523 [11] J. Palmer, R. Mejia-Alvarez, J. Best, and K. Christensen, *Exp. Fluids* **52**, 809 (2012).  
 524 [12] W. Anderson and M. Chamecki, *Physical Review E* **89**, 013005 (2014).  
 525 [13] A. Khosronejad and F. Sotiropoulos, *J. Fluid Mech.* **753**, 150 (2014).  
 526 [14] N. Bristow, G. Blois, J. Best, and K. Christensen, *Journal of Geophysical Research: Earth Surface* (2018).  
 527 [15] N. P. Webb, M. S. Galloza, T. M. Zobeck, and J. E. Herrick, *Aeolian research* **20**, 45 (2016).  
 528 [16] A. B. Smith, D. W. Jackson, and J. A. G. Cooper, *Geomorphology* **278**, 28 (2017).  
 529 [17] S. Leonardi, P. Orlandi, R. Smalley, L. Djenidi, and R. Antonia, *J. Fluid Mech.* **491**, 229 (2003).  
 530 [18] J. Jimenez, *Annu. Rev. Fluid Mech.* **36**, 173 (2004).  
 531 [19] P. R. Owen, *Journal of Fluid Mechanics* **20**, 225 (1964).  
 532 [20] J. Kok, E. Parteli, T. Michaels, and D. Karam, *Reports on Progress in Physics* **75**, 106901:1 (2012).  
 533 [21] T. Pätz, J. Kok, and H. Herrmann, *New Journal of Physics* **14**, 043035 (2012).  
 534 [22] M. P. Almeida, E. J. Parteli, J. S. Andrade, and H. J. Herrmann, *Proceedings of the National Academy of Sciences* **105**,  
 535 6222 (2008).  
 536 [23] R. L. Martin and J. F. Kok, *Science advances* **3**, e1602569 (2017).  
 537 [24] C. Wang, Z. Tang, N. Bristow, G. Blois, K. Christensen, and W. Anderson, *Computers & Fluids* (2016).  
 538 [25] R. Ewing and G. Kocurek, *Geomorphology* **114**, 175 (2010).  
 539 [26] G. Kocurek and R. Ewing, *Geomorphology* **72**, 94 (2005).  
 540 [27] G. Kocurek, M. Carr, R. Ewing, K. Havholm, Y. Nagar, and A. Singhvi, *Sedimentary Geology* **197**, 313 (2007).  
 541 [28] H. Tsoar, *Sedimentology* **30**, 567 (1983).  
 542 [29] N. Lancaster, *Sedimentology* **36**, 273 (1989).  
 543 [30] P. Hersen, K. Andersen, H. Elbelrhiti, B. Andreotti, P. Claudin, and S. Douady, *Phys. Rev. E* **69**, 011304 (2004).  
 544 [31] P. Hersen and S. Douady, *Geophys. Res. Lett.* **32**, doi:10.1029/2005GL024179 (2005).  
 545 [32] E. J. Parteli, O. Durán, M. C. Bourke, H. Tsoar, T. Pöschel, and H. Herrmann, *Aeolian Research* **12**, 121 (2014).  
 546 [33] B. Werner, *Geology* **23**, 1107 (1995).  
 547 [34] B. Andreotti, P. Claudin, and S. Douady, *The European Physical Journal B-Condensed Matter and Complex Systems*  
 548 **28**, 321 (2002).  
 549 [35] B. Andreotti, P. Claudin, and S. Douady, *The European Physical Journal B-Condensed Matter and Complex Systems*  
 550 **28**, 341 (2002).  
 551 [36] B. Andreotti, *Journal of Fluid Mechanics* **510**, 47 (2004).  
 552 [37] B. Andreotti, A. Fourriere, F. Ould-Kaddour, B. Murray, and P. Claudin, *Nature* **457**, 1120 (2009).  
 553 [38] O. Durán, E. J. Parteli, and H. J. Herrmann, *Earth Surface Processes and Landforms* **35**, 1591 (2010).  
 554 [39] E. d. M. FRANKLIN and F. CHARRU, *Journal of Fluid Mechanics* **675**, 199 (2011).  
 555 [40] J. G. Venditti, M. Church, and S. J. Bennett, *Sedimentology* **52**, 1343 (2005).  
 556 [41] J. G. Venditti, M. Church, and S. J. Bennett, *Water resources research* **41** (2005).  
 557 [42] J. G. Venditti, M. A. Church, and S. J. Bennett, *Journal of Geophysical Research: Earth Surface* **110** (2005).  
 558 [43] J. G. Venditti, M. Church, and S. J. Bennett, *Water Resources Research* **42** (2006).  
 559 [44] P. Ortiz and P. K. Smolarkiewicz, *Physical Review E* **79**, 041307 (2009).  
 560 [45] C. Meneveau and J. Katz, *Annual Review of Fluid Mechanics* **32**, 1 (2000).  
 561 [46] J. Albertson and M. Parlange, *Water Resour. Res.* **35**, 2121 (1999).  
 562 [47] W. Anderson and C. Meneveau, *Boundary-Layer Meteorol.* **137**, 397 (2010).  
 563 [48] W. Anderson, *Int. J. Numer. Methods Fluids* **71**, 1588 (2012).

- 564 [49] U. Piomelli and E. Balaras, *Annu. Rev. Fluid Mech.* **34**, 349 (2002).  
565 [50] M. Germano, *J. Fluid Mech.* **238**, 325 (1992).  
566 [51] M. Germano, U. Piomelli, P. Moin, and W. Cabot, *Phys. Fluids A* **3**, 1760 (1991).  
567 [52] E. Bou-Zeid, C. Meneveau, and M. Parlange, *Phys. Fluids* **17**, 025105 (2005).  
568 [53] R. Mittal and G. Iaccarino, *Annual Rev. Fluid Mech.* **37**, 239 (2005).  
569 [54] W. Anderson, Q. Li, and E. Bou-Zeid, *J. Turbulence* **16**, 809 (2015).  
570 [55] W. Anderson, *J. Fluid Mech.* **789**, 567 (2016).  
571 [56] Y. Wu and K. T. Christensen, *J. Fluid Mech.* **655**, 380 (2010).  
572 [57] R. Antonia, *Ann. Rev. of Fluid Mech.* **13**, 131 (1981).  
573 [58] J. Kim, P. Moin, and R. Moser, *J. Fluid Mech.* **177**, 133 (1987).  
574 [59] R. Adrian, in *Zoran P. Zaric Memorial International Seminar on Near-Wall Turbulence* (Hemisphere, 1988).  
575 [60] J. Sheng, E. Malkiel, and J. Katz, *J. Fluid Mech.* **633**, 17 (2009).  
576 [61] J. Finnigan, R. Shaw, and E. Patton, *J. Fluid Mech.* **637**, 387 (2009).  
577 [62] N. Hutchins, J. Monty, B. Ganapathisubramani, H. Ng, and I. Marusic, *J. Fluid Mech.* **673**, 255 (2011).  
578 [63] D. Richter and P. Sullivan, *Physics of Fluids* **26**, 103304 (2014).  
579 [64] C. Jacob and W. Anderson, *Boundary-Layer Meteorology* (2016).  
580 [65] P. Jackson and J. Hunt, *Quarterly Journal of the Royal Meteorological Society* **101**, 929 (1975).  
581 [66] J. Jeong and F. Hussain, *J. Fluid Mech.* **285**, 69 (1995).  
582 [67] K. Christensen and R. Adrian, *J. Fluid Mech.* **431**, 433 (2001).  
583 [68] R. Adrian, *Phys. Fluids* **19**, 041301 (2007).  
584 [69] L. Cohen, *Proc IEEE* **77**, 941 (1989).  
585 [70] M. Farge, *Annu. Rev. Fluid Mech.* **24**, 395 (1992).  
586 [71] M. Omidyeganeh, U. Piomelli, K. T. Christensen, and J. L. Best, *Journal of Geophysical Research: Earth Surface* **118**,  
587 2089 (2013).  
588 [72] H. Perkins, *Journal of Fluid Mechanics* **44**, 721 (1970).  
589 [73] P. Bradshaw, *Ann. Rev. Fluid Mech.* **19**, 53 (1987).  
590 [74] X. Gao, C. Narteau, and O. Rozier, *J. Geophys. Res.-Earth Surf.* **120**, 2200 (2015).